Neuron

Article

Theta Phase Segregation of Input-Specific Gamma Patterns in Entorhinal-Hippocampal Networks

Erik W. Schomburg,[1,2,6] Antonio Fernández-Ruiz,[1,3,6] Kenji Mizuseki,[1,4] Antal Berényi,[1,5] Costas A. Anastassiou,[2,4] Christof Koch,[2,4] and György Buzsáki[1,*]
[1]New York University Neuroscience Institute and Center for Neural Science, New York University, New York, NY 10016, USA
[2]Department of Physics and Division of Biology, California Institute of Technology, Pasadena, CA 91125, USA
[3]School of Physics, Complutense University of Madrid, 28040 Madrid, Spain
[4]Allen Institute for Brain Science, Seattle, WA 98103, USA
[5]MTA-SZTE "Momentum" Oscillatory Neuronal Networks Research Group, Department of Physiology, University of Szeged, Szeged 6720, Hungary
[6]Co-first author
*Correspondence: gyorgy.buzsaki@nyumc.org
http://dx.doi.org/10.1016/j.neuron.2014.08.051

SUMMARY

Precisely how rhythms support neuronal communication remains obscure. We investigated interregional coordination of gamma oscillations using high-density electrophysiological recordings in the rat hippocampus and entorhinal cortex. We found that 30–80 Hz gamma dominated CA1 local field potentials (LFPs) on the descending phase of CA1 theta waves during navigation, with 60–120 Hz gamma at the theta peak. These signals corresponded to CA3 and entorhinal input, respectively. Above 50 Hz, interregional phase-synchronization of principal cell spikes occurred mostly for LFPs in the axonal target domain. CA1 pyramidal cells were phase-locked mainly to fast gamma (>100 Hz) LFP patterns restricted to CA1, which were strongest at the theta trough. While theta phase coordination of spiking across entorhinal-hippocampal regions depended on memory demands, LFP gamma patterns below 100 Hz in the hippocampus were consistently layer specific and largely reflected afferent activity. Gamma synchronization as a mechanism for interregional communication thus rapidly loses efficacy at higher frequencies.

INTRODUCTION

The hippocampal-entorhinal system is characterized by a number of distinct oscillations, including the prominent theta and gamma rhythms (Buzsáki et al., 1983; Bragin et al., 1995; Csicsvari et al., 2003; Colgin et al., 2009; Tort et al., 2009; Canolty and Knight, 2010; Fell and Axmacher, 2011; Buzsáki and Wang, 2012; Belluscio et al., 2012; Lisman and Jensen, 2013; Cabral et al., 2014; Bieri et al., 2014; Igarashi et al., 2014; Yamamoto et al., 2014). An important goal of such investigations is to understand how the rate and timing of spikes in neurons of a downstream network are governed by upstream regions and local interactions and how such interactions support spatial navigation and memory (O'Keefe and Recce, 1993; Hasselmo et al., 2002; Montgomery and Buzsáki, 2007; Mizuseki et al., 2009; Bieri et al., 2014). The local field potential (LFP) can be helpful in this process, provided that its components can be related to individual synaptic sources and the output spiking of specific neuronal populations (Buzsáki et al., 2012; Fernández-Ruiz and Herreras, 2013).

Area CA1 in the hippocampus is under the control of two major upstream regions: area CA3 and the direct entorhinal input from layer 3 (EC3; Witter et al., 1989; Amaral and Witter, 1989). The layer-segregated axon terminals of these inputs mediate both dendritic excitation and feedforward inhibition (Buzsáki, 1984). To determine the theta-gamma timing relationships between the entorhinal and CA3 inputs to the CA1 region, and their impact on the CA1 output, we used high-density extracellular recordings, combined with source separation techniques and unbiased spike-LFP coherence methods, while rats performed different maze tasks and slept in their home cages. We report that CA1 gamma-band LFP patterns and the spike timing of pyramidal cells and interneurons within the theta cycle depended on the relative strengths of the CA3 and EC3 inputs and associated gamma patterns in their target dendritic layers. EC3 input was strongest at the peak of the theta cycle, referenced to the LFP in CA1 stratum pyramidale, and was reflected by a mid-frequency (60–120 Hz) gamma oscillation in the LFP, followed one quarter cycle later by the CA3 input on the descending phase in the form of a transient 30–80 Hz gamma pattern. The relative strength of these signals was strongly influenced by brain state and behavior. Rhythmic input at medium to fast gamma frequencies, however, poorly entrained pyramidal cell spiking. Instead, the output of the CA1 pyramidal cell population was dominated by fast (>100 Hz) oscillations that arose within the CA1 network.

RESULTS

Experiments were carried out while animals ran on a linear track (250 cm long), a T maze, or open field (Mizuseki et al., 2009,2012;
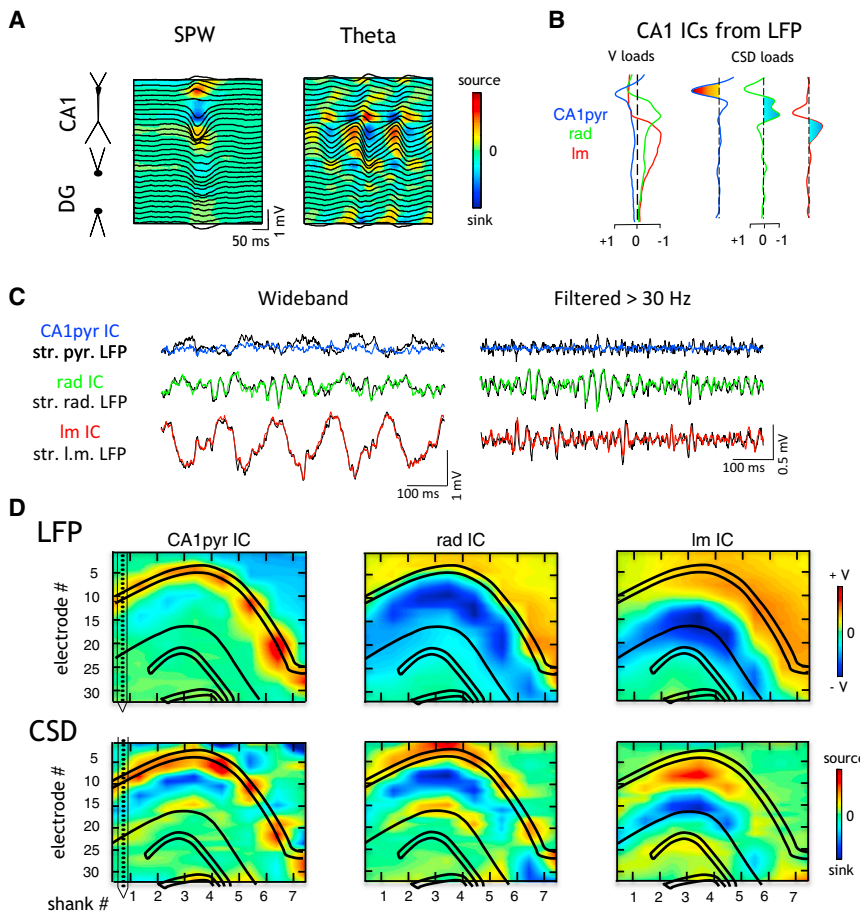
Figure 1. ICA Decomposition of CA1 LFPs Identifies Anatomical Layers

(A) Depth profile of averaged sharp wave (SPW) and theta waves along one shank (32 recording sites, spaced at 50 μm) spanning the CA1 region and dentate gyrus (DG). Traces, LFP; color map, CSD. The strong sink of the SPW corresponds to the str. radiatum, the main termination zone of CA3 afferents.

(B) ICA decomposition of CA1 LFPs into three main components (ICs). The voltage (V) load of the *CA1pyr* ICs (blue trace) peaked at the str. pyramidale. The *rad* IC (green) peaked in the str. radiatum (compare with the source-sink-source distribution of SPW in A). The *lm* IC (red) identified the str. lacunosum-moleculare (compare with the maximum sink of theta in A). CSD loads are the second spatial derivatives of the V loads.

(C) The traces of wide-band (left) and 30 Hz high-pass filtered (right) CA1 ICs and LFPs from the corresponding dendritic layers show a large degree of similarity. The mixing of currents in the pyramidal layer result in greater differences there.

(D) Two-dimensional V and CSD maps of the three main CA1 ICs from a rat with an electrode array spanning the transverse axis of the hippocampus (7 shanks spaced 300 μm; one shank shown on the left). Positive polarity is up in all figures.

position of the individual current generators was performed by one-dimensional current-source density (CSD) analysis of the LFPs recorded on single shanks (Figure 1A; Nicholson and Freeman, 1975). CSD analysis revealed alternating and phase-shifted inward (sink) and outward (source) theta currents in the str. radiatum and lacunosum-moleculare (Buzsáki et al., 1986; Brankack et al., 1993; Montgomery et al., 2009), the major termination zones of the CA3 and EC3 inputs, respectively. The correct identity of layers and current generators was further supported by independent component analysis (ICA) of the multielectrode LFP. ICA discriminates the contributing sources on the basis of their distinct spatial distributions and temporal activations and is less sensitive to spurious sources caused by variability of electrode impedance than CSD methods (see Supplemental Experimental Procedures; Fernández-Ruiz and Herreras, 2013). Applying ICA to each linear shank separated CA1 LFPs into three major pathway-specific independent components (ICs) (Figures 1B–1D and S1). The CSD depth profile of one IC (*rad*) matched the source-sink-source distribution-generated spontaneously occurring sharp waves (SPWs) during immobility, corresponding to strong excitation of CA1 neurons by synchronous CA3 output (Figures 1A and 1B; Bragin et al., 1995; Montgomery and Buzsáki, 2007; Fernández-Ruiz et al., 2012). Another IC (*lm*) corresponded to a current sink in str. lacunosum-moleculare (Figures 1B and 1D; Brankack et al., 1993; Benito et al., 2014), the site of EC3 axon terminals. In contrast to the other two ICs, which were dominated by current sinks in the dendritic layers, the third component (*CA1pyr*) had a current source at the CA1 str. pyramidale (Figures 1B and 1D), which is identifiable by large
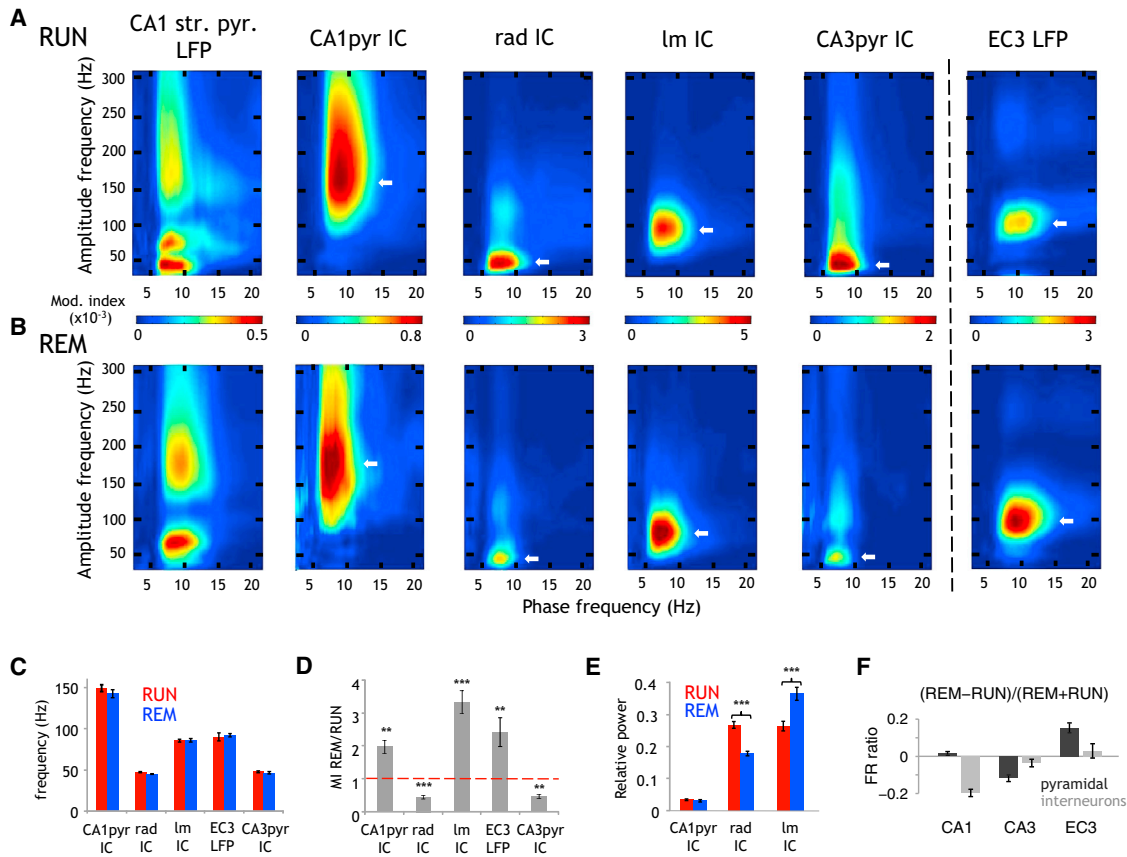
Pastalkova et al., 2008; Diba and Buzsáki, 2008; Montgomery and Buzsáki, 2007; Berényi et al., 2014). Recordings from the hippocampus were made by six- or eight-shank silicon probes covering most layers of CA1 to CA3 and dentate gyrus regions along the transverse axis of the hippocampus (Figures 1D and S1; six rats), allowing us to monitor LFPs from up to 256 sites (Supplemental Experimental Procedures). In separate animals, single unit and LFP recordings were made simultaneously in the CA1 or CA3 pyramidal layer and in multiple layers of the dorso-caudal medial EC (three rats) or CA3 and CA1 pyramidal layers (three rats) using high-density four- or eight-shank silicon probes. Histological localization of the electrodes, criteria for clustering of single units, and separation of principal neurons and interneurons in a subset of these animals have been described in detail previously (Montgomery and Buzsáki, 2007; Sirota et al., 2008; Diba and Buzsáki, 2008; Mizuseki et al., 2009; Berényi et al., 2014). All single units were recorded near the cell body layers, and we therefore included only a subset of the diverse interneuron population (Freund and Buzsáki, 1996; Klausberger and Somogyi, 2008; Fishell and Rudy, 2011). Theta epochs during behavioral tasks were classified as RUN, while those during sleep were classified as rapid eye movement (REM).

Physiological Identification of CA1 Anatomical Layers

The LFP at any point in the brain typically reflects the simultaneous activation of multiple current sinks and sources. Decom-

Figure 2. Spectral Separation of Pathway-Specific Gamma Sub-Bands in CA1

(A) Gamma amplitude-theta frequency (GA-TF) comodulogram of LFP in the CA1 pyramidal layer (CA1 str. pyr. LFP) showed strong theta phase modulation of three gamma sub-bands during RUN (gamma$_S$, gamma$_M$, and gamma$_F$/epsilon; white arrows). Each ICA-derived LFP component (IC) in CA1 displayed modulation in one dominant sub-band. White arrows indicate the frequency of peak power. Note similar gamma frequencies in the *rad* and *CA3pyr* ICs, and the *lm* IC and EC3 LFP, respectively. Color code: strength of GA-TF coupling (modulation index, MI).

(B) Same as in (A) during REM sleep.

(C) Group data of peak frequencies (six rats for CA1 and CA3 ICs, four rats for EC3 LFP).

(D and E) REM/RUN MI ratio (D) and relative power (30–300 Hz) in different layers (E). (*/**/***p < 0.05/0.01/0.001; t test).

(F) Mean ± SEM of firing rate (FR) ratios of single units between REM and RUN ([REM − RUN]/[REM + RUN]).

amplitude ripples and unit firing (Mizuseki et al., 2011). Concatenating and smoothing the one-dimensional IC voltage loadings across shanks resulted in 2D maps showing the layer specificity of each component (Figure 1D; similar layer specificity was found in all six rats). The spectral characteristics of the example traces shown for each component (Figures 1A and S1C) were conserved across entire sessions (Figure S1D).

Layer Distribution and Theta Phase Relationship of Gamma Oscillations

Neural activity is often coordinated on multiple timescales, with interactions between oscillatory processes manifested in cross-frequency coupling (Bragin et al., 1995; Canolty and Knight, 2010; Belluscio et al., 2012; but see Aru et al., 2014). Measuring the modulation of LFP power at higher frequencies (30–300 Hz) by the phase of lower frequency (2–20 Hz) components revealed gamma amplitude-theta frequency (GA-TF) coupling (Tort et al., 2010) in the CA1 pyramidal layer. We

identified three relatively distinct, but overlapping, gamma sub-bands during RUN (Figure 2A; Belluscio et al., 2012), corresponding to slow gamma (gamma$_S$, 30–80 Hz), midfrequency gamma (gamma$_M$, 60–120 Hz), and fast gamma (gamma$_F$, or epsilon band, > 100 Hz). Because LFP gamma currents in the pyramidal layer reflect a combination (in unknown proportions) of active inhibitory currents, passive return currents from the dendritic layers, and spikes (Csicsvari et al., 2003; Glickfeld et al., 2009; Schomburg et al., 2012), we also examined the layer-specific distribution of theta-gamma coupling using ICA. GA-TF analysis of the LFP ICs (Figure 2) revealed significantly theta-modulated gamma bands in all animals (p < 0.001 for each IC/LFP, surrogate test; 12 rats). In the *CA1pyr* IC, theta oscillations most strongly modulated gamma$_F$ frequencies (Figures 2A and 2C; mean ± SEM, 149.4 ± 4.3 Hz). In the *rad* IC, the dominant theta-modulated gamma frequencies were between 30 and 80 Hz (Figures 2A and 2C; 47.3 ± 0.6 Hz), in agreement with a similar gamma band modulation (p > 0.05, t test between
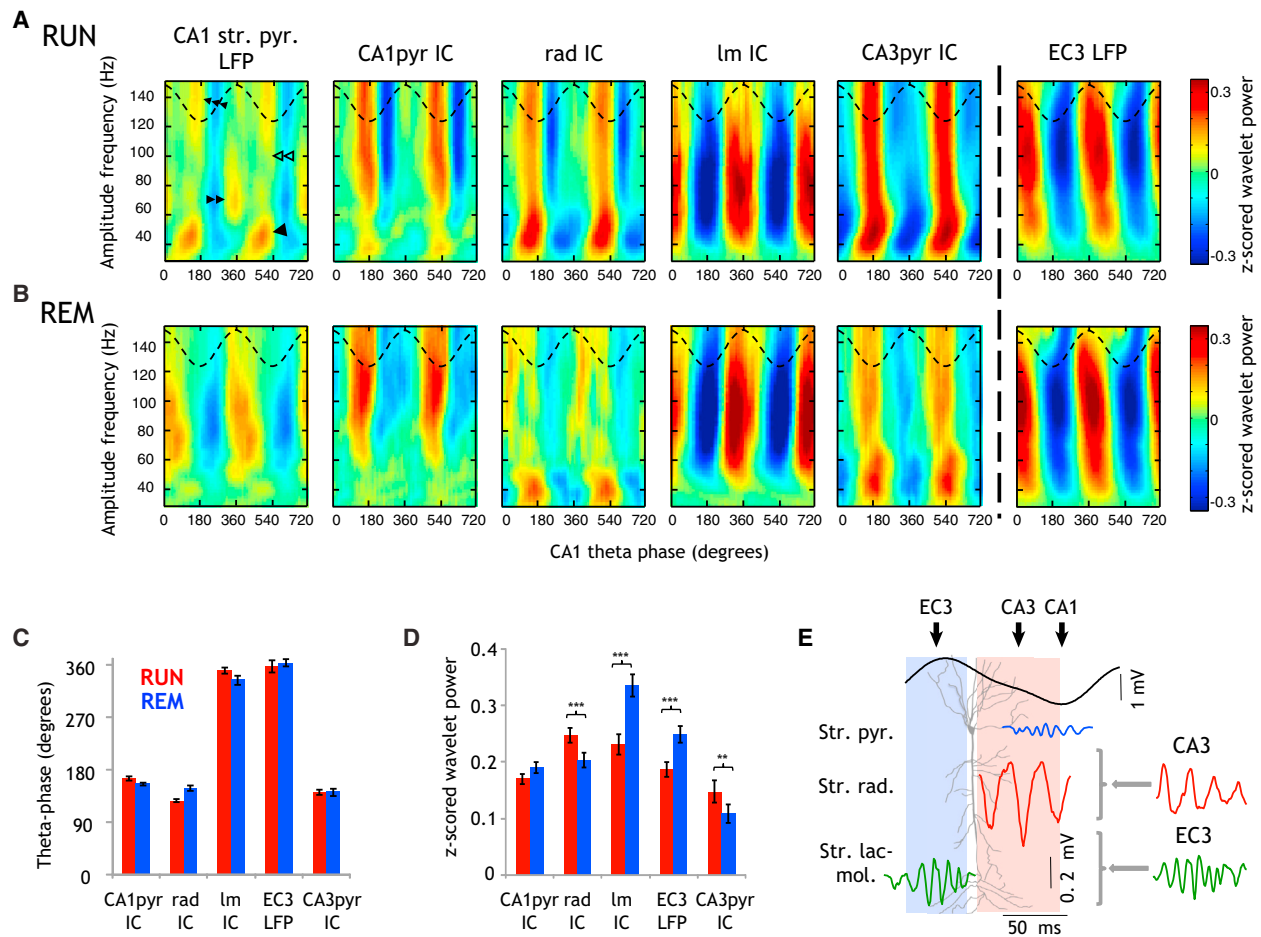
Figure 3. Theta Phase Distribution of CA1 Gamma Oscillations

(A) Gamma amplitude-theta phase (GA-TP) modulation plots of LFP in CA1 pyramidal layer (leftmost panel) and CA1 ICs during RUN. The gamma$_S$ (single arrowhead), gamma$_M$ (double arrowheads), and gamma$_F$ or epsilon (triple arrowhead) dominated the descending phase, peak, and trough of the CA1 pyramidal layer theta waves, respectively. Note that frequency overlaps visible here between phase-separated sub-bands (open double arrowhead) can create artificial boundaries in the GA-TF plots (Figures 2A and 2B). Dashed black line, reference theta phase of the LFP recorded in CA1 pyramidal layer.

(B) Same as in (A) during REM.

(C) Group data (six animals for CA1 and CA3, four rats for EC3) for preferred theta phase of each layer's theta-modulated gamma band (30–60, 60–110, and 100–250 Hz for *rad*, *lm*, and *CA1pyr*, respectively).

(D) Z-scored theta-modulated gamma power across animals. (**/***p < 0.01/0.001, respectively; t test)

(E) Diagram summarizing the average ordering of the maximal phases for the gamma sub-bands, afferent input, and CA1 spike output over the theta cycle.

frequencies) in the CA3 pyramidal layer IC (*CA3pyr*; Figures 2A and 2C; 47.6 ± 1.2 Hz). Compared to the *rad* IC, theta-coupled gamma oscillations in the *lm* IC were significantly faster (p < 0.0001, t test; Figures 2A and 2C; 85.7 ± 1.8 Hz). In the EC3 LFP, the corresponding afferent layer, theta-coupled gamma oscillations were significantly faster than both the *CA3pyr* and CA1 *rad* ICs (p < 0.0001, t test; Figures 2A and 2C; 90.0 ± 4.9 Hz), but not significantly different in peak frequency from the CA1 *lm* IC (p > 0.05, t test). During REM, the frequency distribution of the theta-modulated gamma sub-bands was largely similar to waking (Figures 2B and 2C; p > 0.05, t test). However, the strength of GA-TF coupling (or modulation index, MI) and power of gamma$_S$ in the *rad* IC were significantly reduced during REM compared to RUN (p < 0.0001, t test; Figures 2B, 2D, and 2E), whereas theta-gamma$_M$ coupling and power in the *lm* IC were

significantly increased (p < 0.0001, t test; Figures 2B, 2D, and 2E). These changes were accompanied by a parallel reduction of theta-gamma$_S$ coupling in *CA3pyr* (p < 0.01, t test; Figures 2B and 2D) and increased theta-gamma$_M$ coupling in EC3 LFP during REM (p < 0.01, t test; Figures 2B and 2D). Consistent with the LFP changes, CA3 and EC3 pyramidal neuron firing rates decreased and increased, respectively, during REM compared to RUN (p < 0.05, Kruskal-Wallis ANOVA, followed by Tukey's honestly significant difference test; Figure 2F).

We next examined gamma power variation as a function of theta phase of the LFP recorded from CA1 str. pyramidale (0° and 180° refer to positive polarity peak and negative polarity trough, respectively). This gamma amplitude-theta phase (GA-TP) analysis reinforced the layer preferences of the different gamma sub-bands (Figures 3, S1, and S2). The theta phase
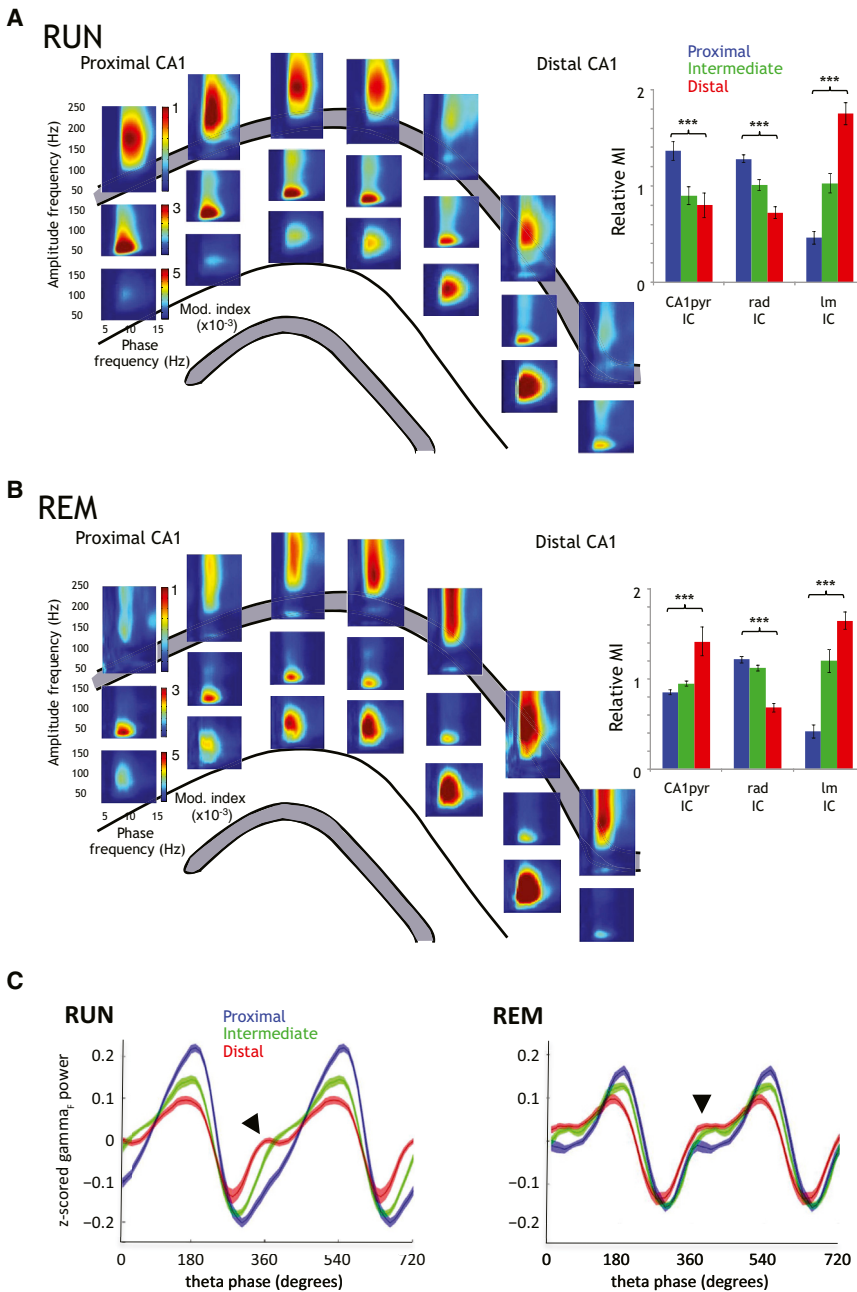
Neuron

Theta-Gamma Coupling in EC-Hippocampal Networks

CellPress

Figure 4. Distribution of Theta-Coupled Gamma Oscillations along the CA1 Transverse Axis of the CA1 Region

(A) Two-dimensional distribution of the theta-coupled gamma oscillations during RUN. Each set of three panels was constructed from the GA-TF coupling of the ICA components (ICs) on each recording shank. The *rad* IC's $gamma_S$ became less theta-modulated along the proximo-distal (i.e., CA3-subicular) axis, whereas *lm* $gamma_M$ increased in coupling strength. *CA1pyr* $gamma_F$ largely followed the *rad* IC gradient. The bar plot on the right shows group data of MIs, normalized by the average across all shanks (six rats). Each comparison showed significant variation from proximal to distal sites (p < 0.001; ANOVA).

(B) Similar display during REM. Note the opposite trend of *CA1pyr* theta-$gamma_F$ coupling along the proximo-distal axis compared to RUN.

(C) Theta phase distribution of *CA1pyr* $gamma_F$ power in RUN and REM at three segments along the proximo-distal axis of CA1. Note increased bimodality of the $gamma_F$ power distribution (arrowheads) toward the distal (subicular) end compared to the CA3 end (p < 0.001 for mean phases both in RUN and REM, ANOVA tests, six rats) and stronger overall bimodality during REM.

Mizuseki et al., 2009). The $gamma_M$ (60–120 Hz) that dominated the *lm* IC was phase-locked to the peak of the reference theta waves (348.8° ± 5.3°; Figures 3A and 3C), coincident with maximal EC3 gamma LFPs (355.8° ± 14.8°; Figures 3A and 3C) and pyramidal cell firing (Mizuseki et al., 2009).

During REM sleep, the theta phase and layer distributions of slow and mid-gamma activity were qualitatively similar to RUN (nonsignificant differences in theta phases of maximal gamma power, p > 0.05, t test; Figures 3B and 3C), but theta-modulated gamma power decreased in the *rad* and *CA3pyr* ICs (p < 0.001, t test) while it increased in the *lm* IC and EC3 LFP (p < 0.0001, t test) during

ordering of gamma patterns (Figures 3A–3C and S2) and the predominant phases of input and output spiking (Mizuseki et al., 2009) during RUN are summarized in Figure 3E (see also the Discussion). $Gamma_F$ power (>100 Hz) in the *CA1pyr* IC was maximal near the trough of the theta cycle (174.8° ± 3.3°; Figures 3A and 3C), coincident with the highest probability of spikes of the CA1 pyramidal neurons at this phase (Buzsáki et al., 1983; Csicsvari et al., 1999; Mizuseki et al., 2009). $Gamma_S$ (30–80 Hz) was most prominent in the *rad* IC, occurring predominantly on the descending phase of theta (mean across animals, 128.3° ± 2.0°; Figures 3A and 3C), which coincides with the gamma oscillations in the *CA3pyr* IC (138.9° ± 4.5°; Figures 3A and 3C) and most CA3 spiking (Csicsvari et al., 2003;

REM (Figures 3B and 3D). $Gamma_F$ (epsilon) power became bimodal in the CA1 pyramidal layer IC and LFP, with power increases at both the trough and peak of CA1 theta cycle (see below, Figure 4), similar to the phase-shifted firing of many CA1 neurons during REM (Mizuseki et al., 2011).

In addition to theta phase and layer differences, the gamma frequency bands were also distinct in their proximo-distal distribution (Figure 4). *Rad* ICs closer to the CA3 region (proximal CA1) showed stronger theta-$gamma_S$ coupling than at sites near the subicular border of the CA1 region (distal CA1), whereas the opposite relationship was observed for the $gamma_M$ band in the *lm* ICs (p < 0.001; ANOVA tests; six rats; Figure 4A). Their frequencies remained constant along the entire transverse

hippocampal axis (Figure S3). During RUN, the *CA1pyr* IC theta-gamma$_F$ coupling was stronger at sites closer to CA3, while it was stronger near the subicular end during REM (p < 0.001, ANOVA tests; Figures 4A and 4B). The changes in *CA1pyr* theta-gamma$_F$ coupling along the proximo-distal axis and between RUN and REM mostly reflected changes in its theta phase distribution. A bimodal phase distribution, exhibiting increased power at both the trough and peak, emerged on the distal end during RUN and at all sites during REM (Figure 4C). The altered phase distributions were limited to the *CA1pyr* ICs; quantifying the phase distribution with the "center of mass" of gamma power showed significant variation for *CA1pyr* from the proximal to distal ends during both RUN and REM (p < 0.001, ANOVA tests; Figure S3), but not for the other components (p > 0.05, ANOVA tests).

Layer-Specific Gamma Rhythms Reflect Distinct Input and Output Patterns

The next level of analysis examined within-layer, cross-layer, and cross-regional interactions among the various gamma oscillations. As a first step, coherence maps in the gamma frequency band were constructed using gamma$_{S,M}$ coherence between LFPs at reference sites in different layers and the remaining 255 channels. This procedure reliably outlined the anatomical layer boundaries in CA1 (Figure 5A). Gamma-band coherence of the ICA components extracted from each shank similarly separated the CA1 layers (Figure 5B; six rats). Gamma coherence remained relatively high (>0.4) for ICs from different shanks but in the same layer, even up to 1.8 mm away, whereas gamma coherence between ICs from different layers was consistently lower, even at the same shank (Figure 5C). Coherence between LFPs recorded from the CA3 and CA1 pyramidal layers showed a peak in the gamma$_S$ band during both RUN and REM (Figure 5D; three rats). LFP coherence between EC3 and the CA1 pyramidal layer was low (<0.1 in each of the three rats) above ∼60 Hz during both RUN and REM. By using wavelet phase coherence, which allows for time-resolved spectral component estimates, we found that the weak but significant coherence between CA1 and EC3 in the gamma$_M$ band was concentrated around the peak of the CA1 str. pyramidale theta LFP.

In several RUN sessions, but not during REM, interregional pairs of LFP signals showed increasing coherence above 100 Hz (Figure 5D). However, additional analyses showed that this long-distance, high-frequency coherence corresponded to a highly synchronous artifact of volume-conducted muscle activity (Figure S4).

In summary, theta-modulated gamma power in the respective dendritic domains of CA1 pyramidal cells mainly reflects the gamma band activity in their respective afferent regions and varied as a function of brain state.

Interneuron Spike to Gamma LFP Phase-Locking Within and Between Regions

The theta phase separation and low cross-layer and cross-regional coherence of LFP gamma waves suggested that afferent gamma patterns arriving to CA1 pyramidal cell dendrites are poorly expressed in the str. pyramidale. We next examined how well LFP oscillations recorded from different locations were reflected in the spike timing of interneurons and pyramidal cells. To provide an unbiased measure of spike phase-locking without arbitrarily prefiltering the LFP, we introduced a wide-band, high-resolution method by calculating the wavelet phase at the time of each spike from 20 to 240 Hz (in logarithmic intervals). Modulation indices were calculated using the mean resulting length of the spike phase vectors, and the significance of phase-locking was assessed using the Rayleigh test on the spike phase distribution with a p < 0.01 threshold (see Supplemental Experimental Procedures).

We examined three types of correlations: (1) intraregional spike-LFP coupling, (2) coupling between spikes in CA3 and EC3 and LFP gamma phases in CA1 (i.e., upstream spikes to downstream LFP), and (3) coupling between the gamma phases of LFPs in CA3 and EC3 and spikes in CA1 (upstream LFP to downstream spikes). To avoid contamination of LFP phase by a unit's spike waveform (Zanos et al., 2011), we measured gamma phases using the LFP recorded 0.4 mm from the unit detection site (i.e., a two-shank gap) in the pyramidal layer (see Figure S6), except in the case of EC3, for which only 0.2 mm separations were available. We first examined the relationship between spikes of putative interneurons in CA1 and LFP at CA1 str. pyramidale, because interneurons, in general, show more reliable phase-locking to afferent patterns than pyramidal cells (Buzsáki et al., 1983; Csicsvari et al., 2003; Brunet et al., 2014). At all frequencies, a large fraction of putative interneurons exhibited significant spike-LFP coupling, but three relatively segregated groups of interneurons emerged during RUN, corresponding approximately to gamma$_S$, gamma$_M$, and gamma$_F$/epsilon bands (Figure 6A). Because individual interneurons could be modulated at multiple gamma frequencies, we report both the fraction of neurons with p values < 0.01 at each frequency band (lines in Figures 6A–6D) and the frequencies with the strongest coupling ("preferred frequency") for those units crossing the p < 0.01 threshold for at least one frequency (bar histograms in Figures 6A–6D). CA3 and EC3 interneurons were also broadly tuned, though EC3 interneurons, preferring mostly high frequencies, were less heterogeneous in their frequency preferences than CA1 or CA3 interneurons. When LFPs were instead taken from CA1 str. radiatum (Figure 6D, first panel), the strongest phase-locking of CA1 interneurons during RUN occurred in the gamma$_S$ band. Similarly, the strongest phase-locking and frequency preferences of CA3 interneurons with CA1 str. radiatum LFP were confined to < 60 Hz (Figure S5). On the other hand, coupling between CA1 interneurons and CA3 pyramidal layer LFP (Figure 6D, second panel) or CA3 interneurons and CA1 pyramidal layer LFP (Figure S5) had a broader distribution of frequency preferences. CA1 interneurons were also phase-locked to gamma frequencies in the EC3 LFP (Figure 6D, third panel) and, in the reverse direction, EC3 interneurons were phase-locked to CA1 LFP gamma (Figure S5), although in significantly lower proportions than between CA3 and CA1 (Figures 6D and S5). Unfortunately, we did not obtain recordings with enough simultaneous single units and str. lacunosum-moleculare LFP for comparable statistics linking them.

The gamma frequency preferences of CA1 interneurons were also related to their theta phase preferences (Figure 6E). Interneurons with gamma$_S$ frequency preferences fired mainly on the descending phase of the theta cycle, whereas both gamma$_M$- and gamma$_F$-preferring units fired most around the
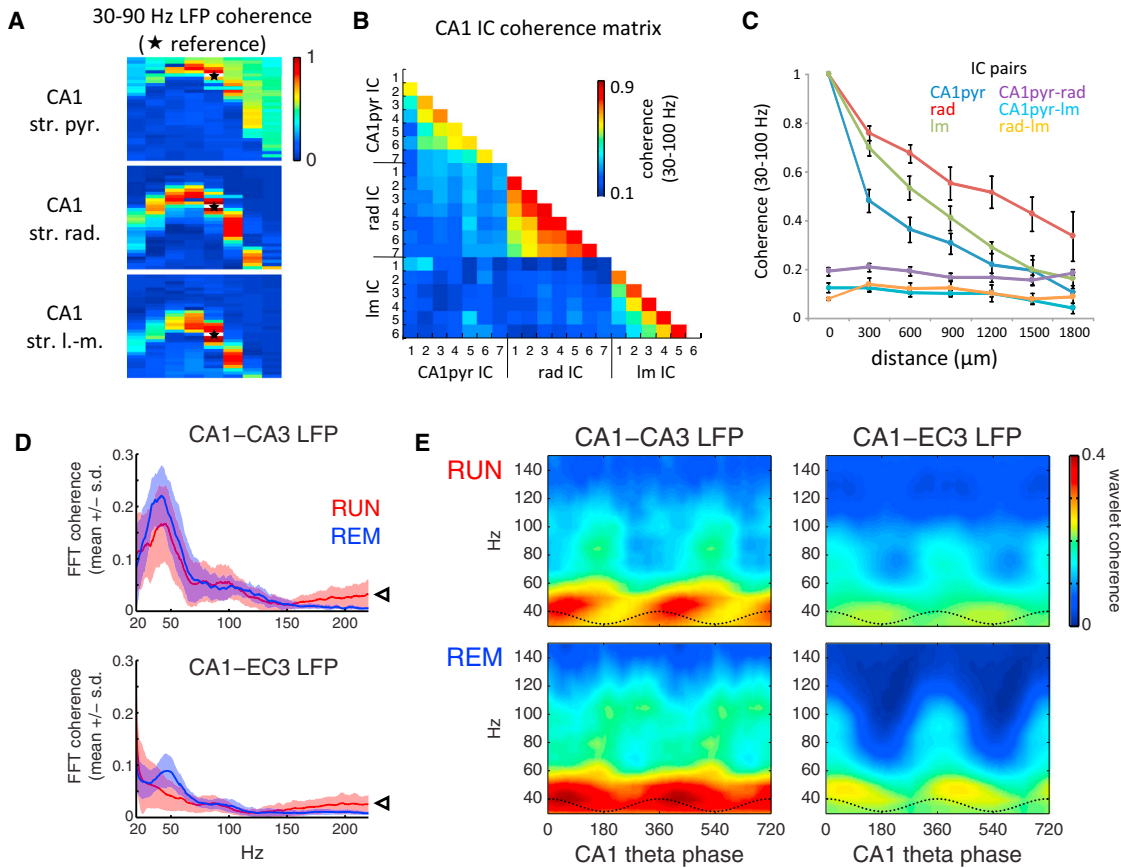
Figure 5. Coherence Segregates Layer-Specific Gamma Generators

(A) Gamma (30–90 Hz) coherence maps between LFP recorded from a reference site (white patch with star) and every other recording site on a 256-channel probe spanning most of a transverse plane in the dorsal hippocampus in one example session, for CA1 str. pyramidale (top), str. radiatum (middle), and str. lacunosum-moleculare (bottom) references.

(B) Gamma coherence between pathway-specific CA1 ICs (extracted separately for each shank). Similar to cross-layer LFP coherence, ICs reflecting different synaptic pathways exhibited low coherence with other CA1 ICs across all shanks (numbered 1–7), but high coherence between like ICs from different shanks.

(C) Coherence of gamma ICs decreased monotonically with distance between shanks, whereas coherence between different ICs was low, regardless of shank separation.

(D) Mean ± SEM of LFP coherence spectra across sessions for RUN and REM between CA1 and CA3 (top, three rats) or CA1 and EC3 (bottom, three rats) site pairs from animals used for the single unit analyses. Coherence increased above 100–150 Hz (arrowheads) due to muscle artifact contamination of LFP recordings (Figure S4).

(E) Mean phase-resolved distributions of wavelet phase coherence over theta cycles in the same animals analyzed in (D). Gamma-band coherence between CA1 and CA3 was more theta-modulated during RUN, when CA3 input was stronger (Figures 2E and 2F) and CA3 gamma oscillations were more theta modulated (Figure 2D). Gamma$_M$ coherence between CA1 and EC3 was highest (double arrowhead) at the phase of maximal EC3 gamma power (Figure 3) and EC3 pyramidal cell spiking (Mizuseki et al., 2009).

trough of the theta waves, respectively, suggesting that the majority of interneurons in the CA1 pyramidal layer are more strongly controlled by CA3 and CA1 pyramidal cells than EC3 inputs. In support of this hypothesis, the gamma$_S$- and gamma$_M$-preferring groups disappeared during REM sleep (Figure 6A, top), during which CA3 pyramidal cells substantially decrease their firing rate (Figure 2F).

Pyramidal Spike to Gamma LFP Phase-Locking Within and Between Regions

Figure 7 summarizes the statistics of pyramidal cell phase-locking in the gamma/epsilon bands within and across regions. CA1 pyramidal cell spikes were moderately coupled to gamma$_S$ frequencies, but much less at gamma$_M$ frequencies, for LFP recorded in the CA1 pyramidal layer during RUN (red traces and histograms). In contrast, they showed strong spike-LFP coupling in the epsilon band (110–200 Hz; Figure 7A). The fractions of pyramidal cells significantly modulated by different gamma bands, on the whole, consistent with most previous studies, which did not characterize frequency preferences in detail (Figure S6D and Table S1). Note that modulation from 20–30 Hz may not be related to gamma activity but instead reflect timing relationships with nonsinusoidal features of theta waves (Belluscio et al., 2012) and/or the third theta harmonic.
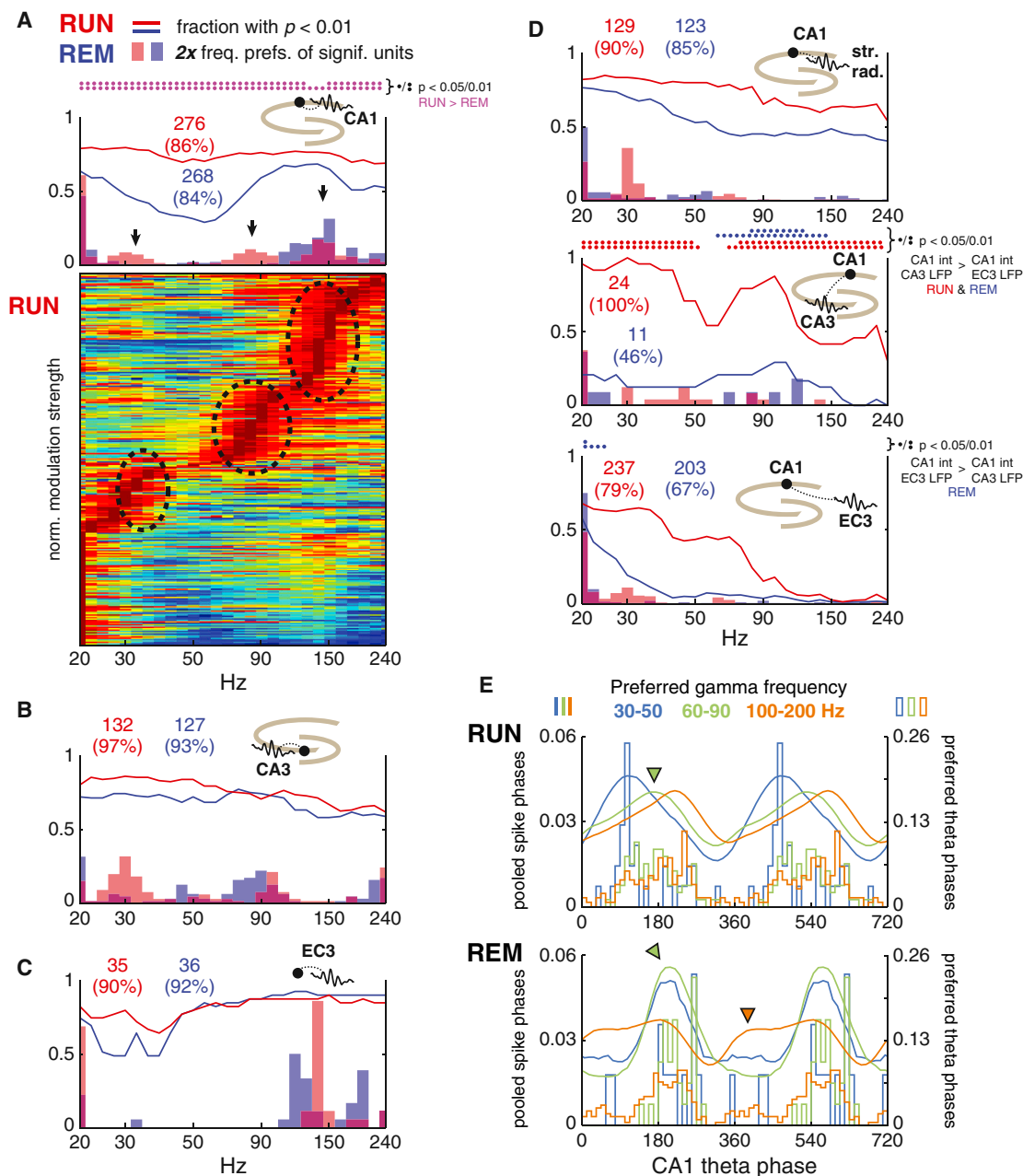
Figure 6. The CA1 Interneuron Population Is Flexibly Modulated by All-Gamma Sub-Bands

(A) Subpopulations of CA1 interneurons were best modulated by different gamma-frequency fluctuations in CA1 LFPs 400 μm away. Plotting the normalized modulation strengths across frequencies for each putative interneuron with a Rayleigh test p value < 0.01 (bottom) revealed groups of interneurons that were most strongly modulated in each gamma sub-band. Overall, individual neurons were typically "significantly" modulated across multiple frequencies (lines, top), with three clear clusters of preferred frequencies (dashed circles and arrows). In this and other panels, significant differences of phase-locking for specific comparisons mentioned in the text are indicated with single (p < 0.05, not adjusted for multiple comparisons) or double (p < 0.01) dotted lines and labeled accordingly.

(B) CA3 interneurons tended to prefer CA3 LFP (400 μm away) frequencies near 30 and 80 Hz.

(C) EC3 interneurons were best modulated at fast gamma frequencies from 100 to 150 Hz relative to EC3 LFPs during both RUN and REM, though this modulation measure may have been biased toward higher frequencies because spike phases were drawn from LFP measured only 200 μm from the unit detection sites.

(D) For LFPs recorded from dendritic (str. radiatum) and afferent sites, CA1 interneurons were best modulated by slow-mid gamma LFP frequencies.

(E) Gamma frequency preferences of CA1 interneurons also segregated neurons by theta phase preference. Units that preferred mid-gamma frequencies fired near the theta trough (green arrowheads), and fast gamma-preferring units only preferred the theta peak during REM (orange arrowhead).
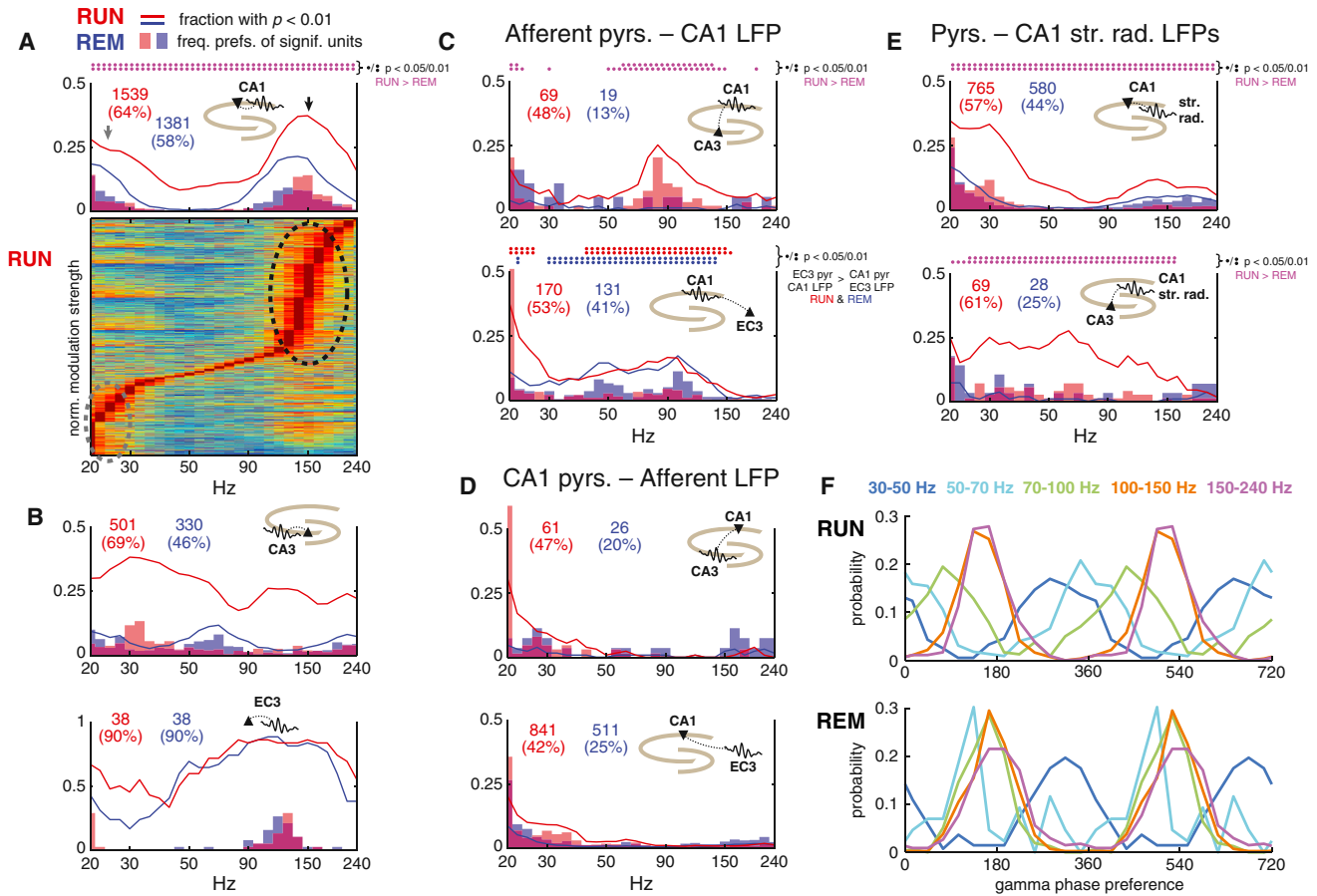
Figure 7. CA1 Pyramidal Cell Spike Timing Was Related to Slow and Fast Gamma Oscillations, but Was Weakly Affected by Mid-Gamma LFP Features.

(A) CA1 pyramidal cells were dominated by fast gamma LFP features (black arrow and dashed circle), even for LFPs 400 μm away (see also Figure S6). Modulation below 30 Hz (gray arrow) may reflect some theta wave asymmetry/harmonic effects. Mid-gamma modulation fell to near chance levels (~1% for p < 0.01 threshold) during REM. Significant differences in phase-locking for specific comparisons mentioned in the text are indicated with dotted lines and labeled accordingly.

(B) Intraregional CA3 (top) and EC3 (bottom) pyramidal cell phase-locking was dominated by the gamma frequencies characteristic of each region (Figure 2).

(C) Spike timing of pyramidal cells in CA3 (top) and EC3 (bottom) was modulated by gamma-band LFP features in CA1.

(D) CA1 pyramidal cell spike timing, however, was substantially influenced by LFPs in afferent regions (CA3, top; EC3, bottom) only at slow gamma frequencies.

(E) CA1 (top) and CA3 (bottom) pyramidal cell phase modulation shifted toward slow gamma when LFP was measured in str. radiatum, suggesting that mid-gamma phase locking of these units in str. pyramidale was due to CA3-driven interneurons in CA1 (see Figures 6 and S5).

(F) Gamma phase preferences (LFP 400 μm away, as in A) of CA1 pyramidal cells shifted from the rising phase to the trough as the gamma frequency preference increased. The slow gamma-like phase distributions present at mid-gamma frequencies during RUN (top) disappeared in REM (bottom).

The distribution of CA1 spike-LFP coupling strengths and frequency preferences was conspicuously different from those that characterized spike-LFP coupling in the CA3 (<75 Hz) and EC3 (70–140 Hz) regions (Figure 7B), reflecting the $gamma_S$ and $gamma_M$ dominance of LFP patterns in each of those regions. When CA1 pyramidal cells were related to LFP recorded in CA3 pyramidal layer or CA1 str. radiatum, the band preferences decreased to mostly below 100 Hz (Figures 7D and 7E), as was the case with interneurons. Likewise, while CA3 pyramidal neurons were preferentially locked to $gamma_S$ in CA1 str. radiatum (Figure 7E), these units were most phase-locked near 80 Hz in CA1 str. pyramidale (Figure 7C), possibly reflecting CA3-driven feedforward perisomatic IPSCs (Figure S5D). Spike-LFP coupling was much stronger in the EC3-to-CA1 direction (Fig-

ure 7C) than in the reverse direction (Figure 7D), especially at $gamma_M$ frequencies, with the percentage of CA1 pyramidal cells locked to EC3 LFPs at frequencies above 80 Hz being less than 3% (i.e., near chance levels).

During REM (Figure 7, blue traces and histograms), CA3 pyramidal cell spike coupling to CA1 LFP gamma oscillation was significantly decreased, congruent with the decreased gamma power in CA1 str. radiatum (Figure 2E) and reduced firing rates of CA3 pyramidal cells (Figure 2F). CA1 pyramidal cells also became significantly less modulated at $gamma_M$ frequencies during REM, consistent with similar changes in the CA1 interneuron population (Figure 6A) and phase-locking between CA3 and CA1 (Figures 6D, 7C, and 7E). This suggests that, despite EC3 input generating $gamma_M$ LFP signals (Figures 2, 3, and

7C), phase-locking of CA1 units to mid-gamma frequencies is dominated by the CA3 input. In support of this hypothesis, the reduction of CA3 input during REM was accompanied by a shift in the preferred $gamma_M$ phases of CA1 pyramidal cell spikes from a $gamma_S$-like distribution to a $gamma_F$-like distribution (Figure 7F).

As an alternate measure of gamma modulation strength across the population, we pooled spike phases across units recorded in all analyzed RUN or REM epochs and calculated the modulation strength and p value (Rayleigh test) for the resulting phase distributions. This method gave qualitatively similar results to those presented above (Figures S6E–S6G). While the pooled spike phases across CA1 pyramidal cells did reach the significance threshold ($p < 0.01$, not corrected for multiple comparisons) for phase locking to EC3 LFP up to 90–95 Hz during RUN and ~140 Hz during REM, it was much weaker than at slow-mid frequencies, or in the reverse direction of EC3 pyramidal cell spikes and CA1 LFP (which was maximal at ~95 Hz). Furthermore, including only spikes occurring when the wavelet power of the LFP was > 2 SD above the mean yielded no noticeable improvement in phase-locking in either the single or pooled unit case (data not shown).

A potential explanation for the relatively weak EC3-CA1 coupling could be that the electrodes in these respective regions were not placed in anatomically connected sites. Our finding of monosynaptic-latency excitation of EC5 interneurons following CA1 pyramidal cell spikes (Figure S5), however, argues against this possibility (Naber et al., 2001). In summary, while spiking in upstream structures was coupled to LFP gamma phase in their target regions, the phase-locking CA1 pyramidal cells to LFP oscillations in afferent regions was typically low and mostly limited to $gamma_S$ frequencies.

Reorganization of CA1 Activity during Memory-Guided Navigation

Brain rhythms are thought to reflect dynamical processes that are functionally related to the cognitive demands of behavior. While we focused here on characterizing the general dynamics of the entorhinal-hippocampal circuit during multiple navigational tasks, we also more specifically examined theta-gamma coupling and unit firing in a hippocampus-dependent delayed-alternation T maze task (Ainge et al., 2007; Montgomery and Buzsáki, 2007; Pastalkova et al., 2008). In this task, rats learned to alternate between turns to the left or right arms on successive trials for water reward (Figures 8A and 8D), with the central arm associated with memory recall (Wood et al., 2000; Montgomery and Buzsáki, 2007). We first compared LFPs in the central and side arms using ICA (Figure 8A; three rats). Both gamma power (Figure S7) and theta-gamma coupling (Figure 8B) were significantly stronger for each CA1 IC during center arm running compared to the side arm, with the largest changes present in CA1 str. radiatum ($p < 0.001$, t test). These behavior-related changes were strongest in the gamma sub-bands that dominate the respective ICs during theta (Figure 8C). Similar to the theta phase distribution shifts from RUN to REM (Figure 4C), the "center of mass" of $gamma_F$ power in the *CA1pyr* IC shifted toward the theta peak in the sides compared to the center arms (Figure S7C), in conjunction with shifted CA1 spiking activity (see below).

We analyzed single unit activity in three additional animals with high-density probes in the hippocampus and entorhinal cortex. We aggregated spikes from each neuron type within each session to compare overall firing rates, because place-specific firing of hippocampal pyramidal cells (O'Keefe and Nadel, 1978) would confound single unit comparisons of firing rates between arms. CA3 pyramidal cell and CA1 interneuron firing rates were significantly greater during center arm running compared to side arms ($p < 0.01$ for CA3 pyramidal cells, $p < 0.05$ for CA1 interneurons, t test on center/side ratios; Figure 8E). As in REM sleep (Figure 2F; Mizuseki et al., 2011), aggregate CA1 pyramidal cell firing rates were not significantly different between maze arms ($p = 0.17$; Figure 8E), but the theta phase distribution of their spikes changed, with more spikes occurring near the peak of CA1 str. pyramidale theta in the side arms compared to in the center arm (Figure 8F), leading to significantly greater theta-modulation of spikes in the center arm compared to the side arms ($p < 0.001$, t test on single unit modulation indices and Wilcoxon rank-sum test on angular dispersion of all spikes). The center-side difference in theta-modulation of EC3 pyramidal cell spikes (Figure 8F) was less stark, only becoming significant ($p < 0.01$) when all spike phases were aggregated together. Theta-modulation scores for single CA3 pyramidal cells showed significantly greater theta modulation in the center arm (when referenced to local theta phase; $p < 0.01$, t test), though the aggregated spike phase distribution was not significantly more modulated. Overall, these experiments demonstrate that the changing balance of CA3 and EC3 inputs during different phases of a hippocampus-dependent memory task can affect the theta organization of both gamma activity and spiking in CA1.

DISCUSSION

Pathway-Specific Gamma Rhythms Are Phase-Coordinated by Theta Oscillations

Our findings support previous observations that $gamma_S$ oscillations occur on the descending phase of theta in the CA1 pyramidal layer (Figure 3), brought about by the gamma-timed spiking of CA3 pyramidal cells and CA1 interneurons (Figures 6A and 7C; Bragin et al., 1995; Csicsvari et al., 2003; Mizuseki et al., 2009; Colgin et al., 2009; Zemankovics et al., 2013), and that this CA3-CA1 gamma coupling is strongest during memory recall (Figure 8; Montgomery and Buzsáki, 2007). A distinct and higher-frequency $gamma_M$ pattern is dominant in the LFP near the peak of the theta cycle (Figure 3; Belluscio et al., 2012), coincident with increased firing of EC3 pyramidal neurons and their excitation of the distal apical dendrites of CA1 pyramidal cells (current sink) (Figure 7C; Mizuseki et al., 2009; Buzsáki et al., 1986). The CA1 output is signaled by increased power above 100 Hz in str. pyramidale (Colgin et al., 2009; Belluscio et al., 2012; Scheffer-Teixeira et al., 2013), and a large fraction of pyramidal neurons are phase-locked to $gamma_F$ patterns in a band-limited manner across several hundred micrometers (Figure 7A). Gamma coherence is high within the same dendritic layer but low across layers (Figure 5; Csicsvari et al., 2003; Montgomery and Buzsáki, 2007).

While the phase and frequency separations between the EC3 and CA3 inputs are consistent with previous reports, our
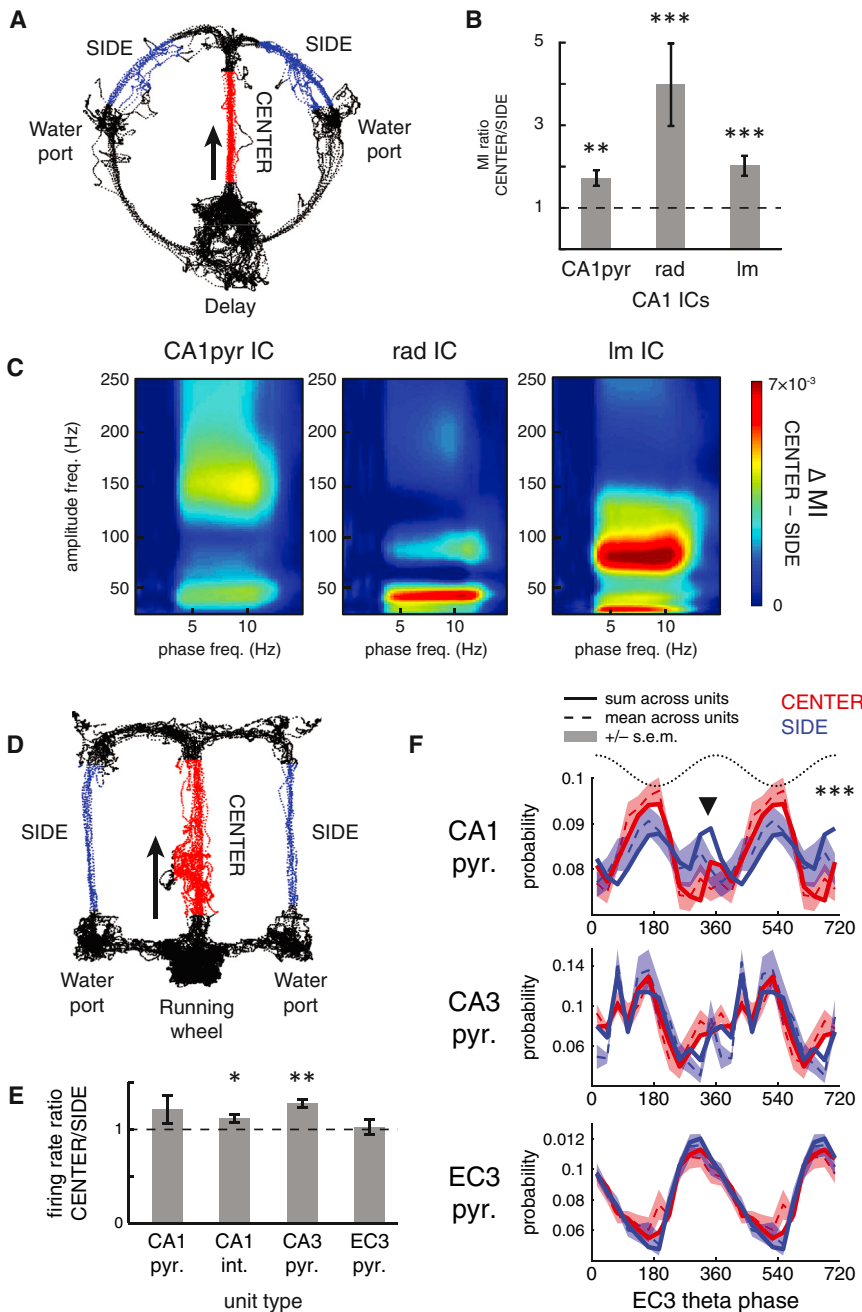
Figure 8. Task-Dependent Changes in CA3-EC3 Input Balance Are Reflected in Theta-Gamma LFP Coupling and CA1 Spiking.

(A) Example running trajectories during one session of a hippocampus-dependent delayed alternation T maze task. We used ICA to compare CA1 LFP components (ICs) during center arm running (CENTER, red) to running in side arms (SIDE, blue).

(B) The theta modulation indices (MI) for CA1 ICs were significantly greater during CENTER running compared to SIDE (t test).

(C) Differences in the theta modulation of the gamma spectra of each IC showed that the strongest changes were at the gamma frequencies characteristic of each afferent pathway (compare Figure 2A).

(D) Example trajectories during one session of a similar delayed alternation task with wheel running during the delay period (Pastalkova et al., 2008), which was performed by the animals used in the unit analyses.

(E) Population firing rate ratios within individual sessions revealed that the CA3 pyramidal cells were significantly more active during CENTER running compared to SIDE (t test). CA1 interneurons also fired at significantly greater rates in CENTER. Across sessions, the measured CA1 and EC3 pyramidal cell population rates were not consistently different in CENTER versus SIDE running (p > 0.05).

(F) Theta phase (EC3 phase reference) distribution of spiking in CA1 (top), CA3 (middle), and EC3 (bottom) pyramidal cell populations during CENTER to SIDE running. Lines show the distribution when spike phases were summed across all clustered pyramidal cells, dashed lines (shading) show mean (±SEM) across single units firing > 30 spikes during CENTER and SIDE epochs. Significance thresholds: */**/***p < 0.05/0.01/0.001.

5E, and 7C), our analysis revealed that such coupling reflected synaptic currents in the dendritic layers but without effectively entraining spikes of pyramidal cells (Figure 7D; see also Lasztóczi and Klausberger, 2014; Yamamoto et al., 2014).

findings are at variance with the postulated theta phase assignment of EC3-mediated gamma bursts by Colgin et al. (2009). In the latter study, the authors suggested that the CA3-driven gamma_S is *followed* by an EC input-driven faster gamma burst in the 65–140 Hz range at the trough of the theta cycle. One potential source of the conflicting results is the use of single site recordings in the Colgin et al. study, which is not sufficient to decompose the spatial origin of the respective gamma generators (Buzsáki et al., 2012; Einevoll et al., 2013; Fernández-Ruiz and Herreras, 2013; Lasztóczi and Klausberger, 2014). While we also found significant phase coupling between entorhinal LFPs and unit spiking and gamma_M LFPs in CA1 (Figures 5D,

In contrast to the framework put forward by Colgin et al. (2009), we find that the maximal firing of EC3 pyramidal cells and the associated gamma_M-band synaptic currents in the CA1 str. lacunosum-moleculare occur, on average, at the peak of the theta cycle (Buzsáki et al., 1986; Brankack et al., 1993; Kamondi et al., 1998; Montgomery et al., 2009; Mizuseki et al., 2009; Benito et al., 2014), *before* the dominant CA3-mediated gamma_S on the descending phase of theta (Figure 3E). Furthermore, the theta phase separation of EC3 spiking (Mizuseki et al., 2009) and gamma oscillations (Figure 3) at the theta peak and the CA1 spiking (Mizuseki et al., 2009) and perisomatic fast-gamma patterns (Figure 3) at the theta trough (Colgin et al., 2009;

Belluscio et al., 2012) imply that fast gamma activity may not be used effectively as a mechanism of communication between CA1 and its afferent regions. Even during REM, when a substantial amount of CA1 spiking (Figure 6E; Mizuseki et al., 2011) and gamma activity (Figure 3B; Belluscio et al., 2012) coincides with EC3 input at the theta peak (Mizuseki et al., 2011), spiking in CA1 was still not coherent with EC3 gamma oscillations (Figure 7D).

Lasztóczi and Klausberger (2014) also implicated EC input to CA1 in generating dendritic (but not perisomatic) synaptic currents, but in the slow gamma band. Their results, however, were obtained under urethane anesthesia, which has been shown to alter EC input to CA1 (Stewart et al., 1992; Buzsáki, 2002). Their recordings in awake mice showed theta-modulated gamma in str. lacunosum-moleculare with similar frequencies to those we found (see also Yamamoto et al., 2014).

Cooperative-Competitive Influence of EC and CA3 on CA1 Output

The firing rate changes of CA3 and EC3 principal cells can at least partially account for the CA1 firing patterns and gamma oscillations we observed both across brain states and in the T maze task. These two major inputs can either cooperate or compete, depending on the nature of the task (Dvorak-Carbone and Schuman, 1999a, 1999b; Remondes and Schuman, 2002; Golding et al., 2002; Dudman et al., 2007; Han and Heinemann, 2013). During the recall phase (center arm) of the T maze task, the CA3 and EC3 inputs may cooperatively increase their influence on CA1 (Montgomery and Buzsáki, 2007; Yamamoto et al., 2014). Properly timed CA3 and EC3 input can also become more effective through suppression of feedforward inhibition (Buzsáki et al., 1995; Yeckel and Berger, 1990; Leão et al., 2012; Basu et al., 2013) or facilitation of mechanisms that can overcome inhibition (Remondes and Schuman, 2002; Jarsky et al., 2005; Takahashi and Magee, 2009).

The competition between the two major pathways was illustrated here during REM sleep and in the T maze side arms, when firing rates of CA3 pyramidal neurons decreased (Figure 2F; Montgomery et al., 2008) in parallel with reductions in the power of gamma$_S$ in CA1 str. radiatum and spike-LFP phase-locking between CA3 pyramidal cells and CA1 LFP (Figures 2, 7C, and 7E). This reduced CA3 output coincides with increased firing of EC3 neurons and elevated gamma$_M$ power in the str. lacunosum-moleculare (Figure 2) and shifted theta phase preferences of a significant fraction of CA1 pyramidal neurons from the trough to the peak (Poe et al., 2000; Mizuseki et al., 2011). Similar mechanisms may also be involved during exploration of a novel environment (Manns et al., 2007; Lever et al., 2010). Additional experiments are required to disentangle the roles of the medial and lateral entorhinal cortical inputs (Hargreaves et al., 2005; Igarashi et al., 2014), as well as working memory-related links to the medial prefrontal cortex through the thalamic nucleus reuniens (Vertes et al., 2007), all of which target str. lacunosum-moleculare.

The increased response of CA1 neurons to the direct EC3 input when CA3 input is diminished can explain why, after lesion of the CA3 input, place-related firing of CA1 pyramidal cells can persist (Brun et al., 2008). The shift in influence can also explain why spatial information encoded by CA1 pyramidal cells varies

as a function of their position in the proximo-distal axis (Figure 4; Henriksen et al., 2010). One potential substrate of the CA3-EC3 competition is the O-LM to bistratified interneuron inhibitory connection. Increased firing of O-LM interneurons near the theta trough (Klausberger and Somogyi, 2008; Varga et al., 2012) suppresses inputs to the distal dendrites, whereas it indirectly disinhibits dendritic segments in str. oriens and radiatum (Leão et al., 2012), thereby facilitating the effectiveness of the CA3 input on CA1 pyramidal cells.

Directionality and Frequency Dependence of Spike-LFP Coupling

The term "spike-LFP coupling" has at least two implied physiological mechanisms: spikes of an upstream network can generate coherent LFP patterns in their target dendritic domains, or, in the reverse direction, oscillations in the upstream network (reflected in the LFP) can be phase-locked to the spikes of the downstream population (Figures 6 and 7). While the former relationship can be strong, we found that the latter is typically weak for pyramidal cells, especially at high frequencies. LFP gamma oscillations in the dendritic layers poorly reflected the timing of the CA1 pyramidal cell spikes (Figure 7), consistent with attenuation and low-pass filtering of distal dendritic currents (Golding et al., 2005; Vaidya and Johnston, 2013), combined with interfering contributions from other excitatory inputs, inhibitory currents, and volume-conducted signals. Additionally, network mechanisms that prevent spike entrainment by incoming gamma bursts may be at work (Pouille and Scanziani, 2001). This is in line with previous in vivo observations showing that even synchronous fast gamma outputs from CA3 often fail to entrain CA1 neurons (Csicsvari et al., 2000; Sullivan et al., 2011; Carr et al., 2012).

While principal cells in the superficial layers of neocortex are more electrotonically compact (Zador et al., 1995), which could perhaps enable cortical circuits to more effectively employ gamma synchronization as a mechanism for selective interregional communication (Singer, 1993; Fries, 2005), this hypothesis remains hotly debated (Shadlen and Movshon, 1999; Kopell et al., 2000; Fries, 2009; Ray and Maunsell, 2010; Fell and Axmacher, 2011; Bosman et al., 2012; Akam and Kullmann, 2012; Jia et al., 2013; Srinath and Ray, 2014). In our analysis, LFP-spike coupling between CA1 units and CA3 or EC3 LFP was mostly attributable to phase-locking of interneurons (Figure 6). Feedforward connections to interneurons (Buzsáki, 1984; Isaacson and Scanziani, 2011), combined with their strong synchronization mechanisms (Galarreta and Hestrin, 2001; Bartos et al., 2007; Hu et al., 2010), could potentially underlie much of the bidirectional gamma synchronization reported across cortical regions (Gregoriou et al., 2009, 2012; Brunet et al., 2014). While we do not rule out that such synchronization may be useful for enhancing synaptic communication, our results do not provide support for fast gamma spike-spike synchronization between principal cells mediating communication between regions.

Yet, a fraction of CA1 pyramidal cells was significantly locked to the phase of str. radiatum gamma rhythms, typically in the slow gamma band (Figure 7E). Such transient coupling is likely to be conveyed primarily by perisomatic interneurons, which have extensive dendritic arbors in the str. radiatum (Freund

and Buzsáki, 1996) and fire preferentially on the descending slope of the theta oscillation (Klausberger and Somogyi, 2008). A potential conduit of gamma coupling between EC3 and CA1 pyramidal cells is the axo-axonic (chandelier) interneuron, since the majority of its dendrites arborize in str. lacunosum-moleculare, and they fire preferentially on the peak of the theta cycle (Klausberger and Somogyi, 2008), coincident with the timing of the EC3 input and emergence of gamma$_M$. Such mechanisms may underlie the weak but significant modulation of multiunit spiking at gamma$_M$ frequencies (Figure S6).

Although interregional transfer of rhythms at high frequencies was poor, a surprisingly large number of CA1 pyramidal cells were phase-locked to the local gamma$_F$/epsilon band. Power increases in this band may reflect a true network oscillation or uncoordinated spiking (Ray and Maunsell, 2011; Belluscio et al., 2012; Schomburg et al., 2012). Spike contamination being the exclusive source of all fast LFP is unlikely, because spike-LFP coupling in the epsilon band was present when LFP was sampled 200–600 μm from the spike detection site (Figure S6). Additional contributions may arrive from concerted IPSCs in the perisomatic region of pyramidal cells, triggered by pyramidal cell spikes (Csicsvari et al., 1998). However, neither spike contamination nor the disynaptic explanation hypothesis explains why local phase locking of spikes in the gamma$_F$/epsilon band is most prominent in the CA1 region during both theta (present findings) and sharp wave ripples (Sullivan et al., 2011; Schomburg et al., 2012). The ripple-frequency synchronization of CA1 pyramidal cells may be a reflection of high-frequency resonance properties of the CA1 circuit (Sullivan et al., 2011; Csicsvari et al., 2000; Brunel and Wang, 2003; Stark et al., 2014).

Overall, our experiments demonstrate that layer-specific gamma oscillations in the hippocampus reliably identify the temporal dynamics of the afferent inputs (spike-LFP coupling). LFP features may therefore aid in identifying processes related to specific memory processes (Montgomery and Buzsáki, 2007; Bieri et al., 2014), but they are poor predictors of interregional coupling of pyramidal cell spikes. Our results instead suggest that temporal coordination (spike-spike coupling) in the entorhinal-hippocampal system is mainly supported by theta and low-mid frequency gamma oscillations, but much less so by fast gamma coherence.

EXPERIMENTAL PROCEDURES

Nine male Long-Evans rats and three male Sprague-Dawley rats (250–400 g, 3–6 months old) were trained in a variety of testing environments and tasks and implanted with movable, multiple-site silicon probes in the dorsal hippocampus, with three of these rats having an additional probe in the dorsocaudal medial entorhinal cortex (EC). Data were recorded while animals performed maze tasks and slept in their home cages. The surgeries, probes, behavioral training, and spike-sorting procedures were described in detail previously (Montgomery and Buzsáki, 2007; Montgomery et al., 2008; Diba and Buzsáki, 2008; Pastalkova et al., 2008; Mizuseki et al., 2009; Berényi et al., 2014). All protocols were approved by the Institutional Animal Care and Use Committee of New York University.

Synaptic current generators were decomposed using CSD and ICA of the LFPs (Fernández-Ruiz et al., 2012). Spectro-temporal analyses of the activation strengths of IC extracted from LFPs are indicated by their IC labels (e.g., *CA1pyr*, *rad*, *lm*), and analyses on LFPs are labeled by their anatomical location (CA1 str. pyr., str. rad., etc.). Epochs of high theta (4–10 Hz) power

during locomotion were classified as RUN. Theta episodes during sleep were classified as REM. Time-resolved spectral decomposition of time series data was performed using wavelet analysis. Theta phase analyses of wavelet spectra and unit spiking used the phase extracted from the Hilbert transform of the 4–12 Hz filtered CA1 str. pyramidale LFP. Subsets of the 32- to 64-electrode recordings are available in the hc-3 data set at http://crcns.org (Mizuseki et al., 2014). Further details and discussion of the recordings and data analyses are available as Supplemental Experimental Procedures.

REFERENCES

Ainge, J.A., van der Meer, M.A.A., Langston, R.F., and Wood, E.R. (2007). Exploring the role of context-dependent hippocampal activity in spatial alternation behavior. Hippocampus *17*, 988–1002.

Akam, T.E., and Kullmann, D.M. (2012). Efficient "communication through coherence" requires oscillations structured to minimize interference between signals. PLoS Comput. Biol. *8*, e1002760.

Amaral, D.G., and Witter, M.P. (1989). The three-dimensional organization of the hippocampal formation: a review of anatomical data. Neuroscience *31*, 571–591.

Aru, J., Aru, J., Priesemann, V., Wibral, M., Lana, L., Pipa, G., Singer, W., and Vicente, R. (2014) Untangling cross-frequency coupling in neuroscience. arXiv, arXiv:1405.7965, http://arxiv.org/abs/1405.7965.

Bartos, M., Vida, I., and Jonas, P. (2007). Synaptic mechanisms of synchronized gamma oscillations in inhibitory interneuron networks. Nat. Rev. Neurosci. *8*, 45–56.

Basu, J., Srinivas, K.V., Cheung, S.K., Taniguchi, H., Huang, Z.J., and Siegelbaum, S.A. (2013). A cortico-hippocampal learning rule shapes inhibitory microcircuit activity to enhance hippocampal information flow. Neuron *79*, 1208–1221.

Belluscio, M.A., Mizuseki, K., Schmidt, R., Kempter, R., and Buzsáki, G. (2012). Cross-frequency phase-phase coupling between θ and γ oscillations in the hippocampus. J. Neurosci. *32*, 423–435.

Benito, N., Fernández-Ruiz, A., Makarov, V.A., Makarova, J., Korovaichuk, A., and Herreras, O. (2014). Spatial modules of coherent activity in pathway-specific LFPs in the hippocampus reflect topology and different modes of presynaptic synchronization. Cereb. Cortex *24*, 1738–1752.

Berényi, A., Somogyvári, Z., Nagy, A.J., Roux, L., Long, J.D., Fujisawa, S., Stark, E., Leonardo, A., Harris, T.D., and Buzsáki, G. (2014). Large-scale, high-density (up to 512 channels) recording of local circuits in behaving animals. J. Neurophysiol. *111*, 1132–1149.

Bieri, K.W., Bobbitt, K.N., and Colgin, L.L. (2014). Slow and fast γ rhythms coordinate different spatial coding modes in hippocampal place cells. Neuron *82*, 670–681.

Bosman, C.A., Schoffelen, J.-M., Brunet, N., Oostenveld, R., Bastos, A.M., Womelsdorf, T., Rubehn, B., Stieglitz, T., De Weerd, P., and Fries, P. (2012). Attentional stimulus selection through selective synchronization between monkey visual areas. Neuron *75*, 875–888.

Bragin, A., Jandó, G., Nádasdy, Z., Hetke, J., Wise, K., and Buzsáki, G. (1995). Gamma (40-100 Hz) oscillation in the hippocampus of the behaving rat. J. Neurosci. *15*, 47–60.

Brankack, J., Stewart, M., and Fox, S.E. (1993). Current source density analysis of the hippocampal theta rhythm: associated sustained potentials and candidate synaptic generators. Brain Res. *615*, 310–327.

Brun, V.H., Leutgeb, S., Wu, H.-Q., Schwarcz, R., Witter, M.P., Moser, E.I., and Moser, M.-B. (2008). Impaired spatial representation in CA1 after lesion of direct input from entorhinal cortex. Neuron *57*, 290–302.

Brunel, N., and Wang, X.J. (2003). What determines the frequency of fast network oscillations with irregular neural discharges? I. Synaptic dynamics and excitation-inhibition balance. J. Neurophysiol. *90*, 415–430.

Brunet, N.M., Bosman, C.A., Vinck, M., Roberts, M., Oostenveld, R., Desimone, R., De Weerd, P., and Fries, P. (2014). Stimulus repetition modulates gamma-band synchronization in primate visual cortex. Proc. Natl. Acad. Sci. USA *111*, 3626–3631.

Buzsáki, G. (1984). Feed-forward inhibition in the hippocampal formation. Prog. Neurobiol. *22*, 131–153.

Buzsáki, G. (2002). Theta oscillations in the hippocampus. Neuron *33*, 325–340.

Buzsáki, G., and Wang, X.-J. (2012). Mechanisms of gamma oscillations. Annu. Rev. Neurosci. *35*, 203–225.

Buzsáki, G., Leung, L.W., and Vanderwolf, C.H. (1983). Cellular bases of hippocampal EEG in the behaving rat. Brain Res. *287*, 139–171.

Buzsáki, G., Czopf, J., Kondákor, I., and Kellényi, L. (1986). Laminar distribution of hippocampal rhythmic slow activity (RSA) in the behaving rat: current-source density analysis, effects of urethane and atropine. Brain Res. *365*, 125–137.

Buzsáki, G., Penttonen, M., Bragin, A., Nádasdy, Z., and Chrobak, J.J. (1995). Possible physiological role of the perforant path-CA1 projection. Hippocampus *5*, 141–146.

Buzsáki, G., Anastassiou, C.A., and Koch, C. (2012). The origin of extracellular fields and currents—EEG, ECoG, LFP and spikes. Nat. Rev. Neurosci. *13*, 407–420.

Cabral, H.O., Vinck, M., Fouquet, C., Pennartz, C.M.A., Rondi-Reig, L., and Battaglia, F.P. (2014). Oscillatory dynamics and place field maps reflect hippocampal ensemble processing of sequence and place memory under NMDA receptor control. Neuron *81*, 402–415.

Canolty, R.T., and Knight, R.T. (2010). The functional role of cross-frequency coupling. Trends Cogn. Sci. *14*, 506–515.

Carr, M.F., Karlsson, M.P., and Frank, L.M. (2012). Transient slow gamma synchrony underlies hippocampal memory replay. Neuron *75*, 700–713.

Colgin, L.L., Denninger, T., Fyhn, M., Hafting, T., Bonnevie, T., Jensen, O., Moser, M.-B., and Moser, E.I. (2009). Frequency of gamma oscillations routes flow of information in the hippocampus. Nature *462*, 353–357.

Csicsvari, J., Hirase, H., Czurko, A., and Buzsáki, G. (1998). Reliability and state dependence of pyramidal cell–interneuron synapses in the hippocampus: an ensemble approach in the behaving rat. Neuron *21*, 179–189.

Csicsvari, J., Hirase, H., Czurkó, A., Mamiya, A., and Buzsáki, G. (1999). Oscillatory coupling of hippocampal pyramidal cells and interneurons in the behaving Rat. J. Neurosci. *19*, 274–287.

Csicsvari, J., Hirase, H., Mamiya, A., and Buzsáki, G. (2000). Ensemble patterns of hippocampal CA3-CA1 neurons during sharp wave-associated population events. Neuron *28*, 585–594.

Csicsvari, J., Jamieson, B., Wise, K.D., and Buzsáki, G. (2003). Mechanisms of gamma oscillations in the hippocampus of the behaving rat. Neuron *37*, 311–322.

Diba, K., and Buzsáki, G. (2008). Hippocampal network dynamics constrain the time lag between pyramidal cells across modified environments. J. Neurosci. *28*, 13448–13456.

Dudman, J.T., Tsay, D., and Siegelbaum, S.A. (2007). A role for synaptic inputs at distal dendrites: instructive signals for hippocampal long-term plasticity. Neuron *56*, 866–879.

Dvorak-Carbone, H., and Schuman, E.M. (1999a). Long-term depression of temporoammonic-CA1 hippocampal synaptic transmission. J. Neurophysiol. *81*, 1036–1044.

Dvorak-Carbone, H., and Schuman, E.M. (1999b). Patterned activity in stratum lacunosum moleculare inhibits CA1 pyramidal neuron firing. J. Neurophysiol. *82*, 3213–3222.

Einevoll, G.T., Kayser, C., Logothetis, N.K., and Panzeri, S. (2013). Modelling and analysis of local field potentials for studying the function of cortical circuits. Nat. Rev. Neurosci. *14*, 770–785.

Fell, J., and Axmacher, N. (2011). The role of phase synchronization in memory processes. Nat. Rev. Neurosci. *12*, 105–118.

Fernández-Ruiz, A., and Herreras, O. (2013). Identifying the synaptic origin of ongoing neuronal oscillations through spatial discrimination of electric fields. Front Comput Neurosci *7*, 5.

Fernández-Ruiz, A., Makarov, V.A., Benito, N., and Herreras, O. (2012). Schaffer-specific local field potentials reflect discrete excitatory events at gamma frequency that may fire postsynaptic hippocampal CA1 units. J. Neurosci. *32*, 5165–5176.

Fishell, G., and Rudy, B. (2011). Mechanisms of inhibition within the telencephalon: "where the wild things are". Ann. Rev. Neurosci. *34*, 535–567.

Freund, T.F., and Buzsáki, G. (1996). Interneurons of the hippocampus. Hippocampus *6*, 347–470.

Fries, P. (2005). A mechanism for cognitive dynamics: neuronal communication through neuronal coherence. Trends Cogn. Sci. *9*, 474–480.

Fries, P. (2009). Neuronal gamma-band synchronization as a fundamental process in cortical computation. Annu. Rev. Neurosci. *32*, 209–224.

Galarreta, M., and Hestrin, S. (2001). Spike transmission and synchrony detection in networks of GABAergic interneurons. Science *292*, 2295–2299.

Glickfeld, L.L., Roberts, J.D., Somogyi, P., and Scanziani, M. (2009). Interneurons hyperpolarize pyramidal cells along their entire somatodendritic axis. Nat. Neurosci. *12*, 21–23.

Golding, N.L., Staff, N.P., and Spruston, N. (2002). Dendritic spikes as a mechanism for cooperative long-term potentiation. Nature *418*, 326–331.

Golding, N.L., Mickus, T.J., Katz, Y., Kath, W.L., and Spruston, N. (2005). Factors mediating powerful voltage attenuation along CA1 pyramidal neuron dendrites. J. Physiol. *568*, 69–82.

Gregoriou, G.G., Gotts, S.J., Zhou, H., and Desimone, R. (2009). High-frequency, long-range coupling between prefrontal and visual cortex during attention. Science *324*, 1207–1210.

Gregoriou, G.G., Gotts, S.J., and Desimone, R. (2012). Cell-type-specific synchronization of neural activity in FEF with V4 during attention. Neuron *73*, 581–594.

Han, E.B., and Heinemann, S.F. (2013). Distal dendritic inputs control neuronal activity by heterosynaptic potentiation of proximal inputs. J. Neurosci. *33*, 1314–1325.

Hargreaves, E.L., Rao, G., Lee, I., and Knierim, J.J. (2005). Major dissociation between medial and lateral entorhinal input to dorsal hippocampus. Science *308*, 1792–1794.

Hasselmo, M.E., Bodelón, C., and Wyble, B.P. (2002). A proposed function for hippocampal theta rhythm: separate phases of encoding and retrieval enhance reversal of prior learning. Neural Comput. *14*, 793–817.

Henriksen, E.J., Colgin, L.L., Barnes, C.A., Witter, M.P., Moser, M.-B., and Moser, E.I. (2010). Spatial representation along the proximodistal axis of CA1. Neuron *68*, 127–137.

Hu, H., Martina, M., and Jonas, P. (2010). Dendritic mechanisms underlying rapid synaptic activation of fast-spiking hippocampal interneurons. Science *327*, 52–58.

Igarashi, K.M., Lu, L., Colgin, L.L., Moser, M.-B., and Moser, E.I. (2014). Coordination of entorhinal-hippocampal ensemble activity during associative learning. Nature *510*, 143–147.

Isaacson, J.S., and Scanziani, M. (2011). How inhibition shapes cortical activity. Neuron *72*, 231–243.

Jarsky, T., Roxin, A., Kath, W.L., and Spruston, N. (2005). Conditional dendritic spike propagation following distal synaptic activation of hippocampal CA1 pyramidal neurons. Nat. Neurosci. *8*, 1667–1676.

Jia, X., Tanabe, S., and Kohn, A. (2013). γ and the coordination of spiking activity in early visual cortex. Neuron *77*, 762–774.

Kamondi, A., Acsády, L., Wang, X.J., and Buzsáki, G. (1998). Theta oscillations in somata and dendrites of hippocampal pyramidal cells in vivo: activity-dependent phase-precession of action potentials. Hippocampus *8*, 244–261.

Klausberger, T., and Somogyi, P. (2008). Neuronal diversity and temporal dynamics: the unity of hippocampal circuit operations. Science *321*, 53–57.

Kopell, N., Ermentrout, G.B., Whittington, M.A., and Traub, R.D. (2000). Gamma rhythms and beta rhythms have different synchronization properties. Proc. Natl. Acad. Sci. USA *97*, 1867–1872.

Lasztóczi, B., and Klausberger, T. (2014). Layer-specific GABAergic control of distinct gamma oscillations in the CA1 hippocampus. Neuron *81*, 1126–1139.

Leão, R.N., Mikulovic, S., Leão, K.E., Munguba, H., Gezelius, H., Enjin, A., Patra, K., Eriksson, A., Loew, L.M., Tort, A.B.L., and Kullander, K. (2012). OLM interneurons differentially modulate CA3 and entorhinal inputs to hippocampal CA1 neurons. Nat. Neurosci. *15*, 1524–1530.

Lever, C., Burton, S., Jeewajee, A., Wills, T.J., Cacucci, F., Burgess, N., and O'Keefe, J. (2010). Environmental novelty elicits a later theta phase of firing in CA1 but not subiculum. Hippocampus *20*, 229–234.

Lisman, J.E., and Jensen, O. (2013). The θ-γ neural code. Neuron *77*, 1002–1016.

Manns, J.R., Zilli, E.A., Ong, K.C., Hasselmo, M.E., and Eichenbaum, H. (2007). Hippocampal CA1 spiking during encoding and retrieval: relation to theta phase. Neurobiol. Learn. Mem. *87*, 9–20.

Mizuseki, K., Sirota, A., Pastalkova, E., and Buzsáki, G. (2009). Theta oscillations provide temporal windows for local circuit computation in the entorhinal-hippocampal loop. Neuron *64*, 267–280.

Mizuseki, K., Diba, K., Pastalkova, E., and Buzsáki, G. (2011). Hippocampal CA1 pyramidal cells form functionally distinct sublayers. Nat. Neurosci. *14*, 1174–1181.

Mizuseki, K., Royer, S., Diba, K., and Buzsáki, G. (2012). Activity dynamics and behavioral correlates of CA3 and CA1 hippocampal pyramidal neurons. Hippocampus *22*, 1659–1680.

Mizuseki, K., Diba, K., Pastalkova, E., Teeters, J., Sirota, A., and Buzsáki, G. (2014). Neurosharing: large-scale data sets (spike, LFP) recorded from the hippocampal-entorhinal system in behaving rats. F1000Res *3*, 98.

Montgomery, S.M., and Buzsáki, G. (2007). Gamma oscillations dynamically couple hippocampal CA3 and CA1 regions during memory task performance. Proc. Natl. Acad. Sci. USA *104*, 14495–14500.

Montgomery, S.M., Sirota, A., and Buzsáki, G. (2008). Theta and gamma coordination of hippocampal networks during waking and rapid eye movement sleep. J. Neurosci. *28*, 6731–6741.

Montgomery, S.M., Betancur, M.I., and Buzsáki, G. (2009). Behavior-dependent coordination of multiple theta dipoles in the hippocampus. J. Neurosci. *29*, 1381–1394.

Naber, P.A., Lopes da Silva, F.H., and Witter, M.P. (2001). Reciprocal connections between the entorhinal cortex and hippocampal fields CA1 and the subiculum are in register with the projections from CA1 to the subiculum. Hippocampus *11*, 99–104.

Nicholson, C., and Freeman, J.A. (1975). Theory of current source-density analysis and determination of conductivity tensor for anuran cerebellum. J. Neurophysiol. *38*, 356–368.

O'Keefe, J., and Nadel, L. (1978). The Hippocampus as a Cognitive Map. (Oxford: Clarendon Press).

O'Keefe, J., and Recce, M.L. (1993). Phase relationship between hippocampal place units and the EEG theta rhythm. Hippocampus *3*, 317–330.

Pastalkova, E., Itskov, V., Amarasingham, A., and Buzsáki, G. (2008). Internally generated cell assembly sequences in the rat hippocampus. Science *321*, 1322–1327.

Poe, G.R., Nitz, D.A., McNaughton, B.L., and Barnes, C.A. (2000). Experience-dependent phase-reversal of hippocampal neuron firing during REM sleep. Brain Res. *855*, 176–180.

Pouille, F., and Scanziani, M. (2001). Enforcement of temporal fidelity in pyramidal cells by somatic feed-forward inhibition. Science *293*, 1159–1163.

Ray, S., and Maunsell, J.H.R. (2010). Differences in gamma frequencies across visual cortex restrict their possible use in computation. Neuron *67*, 885–896.

Ray, S., and Maunsell, J.H.R. (2011). Different origins of gamma rhythm and high-gamma activity in macaque visual cortex. PLoS Biol. *9*, e1000610.

Remondes, M., and Schuman, E.M. (2002). Direct cortical input modulates plasticity and spiking in CA1 pyramidal neurons. Nature *416*, 736–740.

Scheffer-Teixeira, R., Belchior, H., Leão, R.N., Ribeiro, S., and Tort, A.B.L. (2013). On high-frequency field oscillations (>100 Hz) and the spectral leakage of spiking activity. J. Neurosci. *33*, 1535–1539.

Schomburg, E.W., Anastassiou, C.A., Buzsáki, G., and Koch, C. (2012). The spiking component of oscillatory extracellular potentials in the rat hippocampus. J. Neurosci. *32*, 11798–11811.

Shadlen, M.N., and Movshon, J.A. (1999). Synchrony unbound: a critical evaluation of the temporal binding hypothesis. Neuron *24*, 67–77, 111–125.

Singer, W. (1993). Synchronization of cortical activity and its putative role in information processing and learning. Annu. Rev. Physiol. *55*, 349–374.

Sirota, A., Montgomery, S., Fujisawa, S., Isomura, Y., Zugaro, M., and Buzsáki, G. (2008). Entrainment of neocortical neurons and gamma oscillations by the hippocampal theta rhythm. Neuron *60*, 683–697.

Srinath, R., and Ray, S. (2014). Effect of amplitude correlations on coherence in the local field potential. J. Neurophysiol. *112*, 741–751.

Stark, E., Roux, L., Eichler, R., Senzai, Y., Royer, S., and Buzsáki, G. (2014). Pyramidal cell-interneuron interactions underlie hippocampal ripple oscillations. Neuron *83*, 467–480.

Stewart, M., Quirk, G.J., Barry, M., and Fox, S.E. (1992). Firing relations of medial entorhinal neurons to the hippocampal theta rhythm in urethane anesthetized and walking rats. Exp. Brain Res. *90*, 21–28.

Sullivan, D., Csicsvari, J., Mizuseki, K., Montgomery, S., Diba, K., and Buzsáki, G. (2011). Relationships between hippocampal sharp waves, ripples, and fast gamma oscillation: influence of dentate and entorhinal cortical activity. J. Neurosci. *31*, 8605–8616.

Takahashi, H., and Magee, J.C. (2009). Pathway interactions and synaptic plasticity in the dendritic tuft regions of CA1 pyramidal neurons. Neuron *62*, 102–111.

Tort, A.B.L., Komorowski, R.W., Manns, J.R., Kopell, N.J., and Eichenbaum, H. (2009). Theta-gamma coupling increases during the learning of item-context associations. Proc. Natl. Acad. Sci. USA *106*, 20942–20947.

Tort, A.B.L., Komorowski, R., Eichenbaum, H., and Kopell, N. (2010). Measuring phase-amplitude coupling between neuronal oscillations of different frequencies. J. Neurophysiol. *104*, 1195–1210.

Vaidya, S.P., and Johnston, D. (2013). Temporal synchrony and gamma-to-theta power conversion in the dendrites of CA1 pyramidal neurons. Nat. Neurosci. *16*, 1812–1820.

Varga, C., Golshani, P., and Soltesz, I. (2012). Frequency-invariant temporal ordering of interneuronal discharges during hippocampal oscillations in awake mice. Proc. Natl. Acad. Sci. USA *109*, E2726–E2734.

Vertes, R.P., Hoover, W.B., Szigeti-Buck, K., and Leranth, C. (2007). Nucleus reuniens of the midline thalamus: link between the medial prefrontal cortex and the hippocampus. Brain Res. Bull. *71*, 601–609.

Witter, M.P., Groenewegen, H.J., Lopes da Silva, F.H., and Lohman, A.H. (1989). Functional organization of the extrinsic and intrinsic circuitry of the parahippocampal region. Prog. Neurobiol. *33*, 161–253.

Wood, E.R., Dudchenko, P.A., Robitsek, R.J., and Eichenbaum, H. (2000). Hippocampal neurons encode information about different types of memory episodes occurring in the same location. Neuron *27*, 623–633.

Yamamoto, J., Suh, J., Takeuchi, D., and Tonegawa, S. (2014). Successful execution of working memory linked to synchronized high-frequency gamma oscillations. Cell *157*, 845–857.

Yeckel, M.F., and Berger, T.W. (1990). Feedforward excitation of the hippocampus by afferents from the entorhinal cortex: redefinition of the role of the trisynaptic pathway. Proc. Natl. Acad. Sci. USA *87*, 5832–5836.

Zador, A.M., Agmon-Snir, H., and Segev, I. (1995). The morphoelectrotonic transform: a graphical approach to dendritic function. J. Neurosci. *15*, 1669–1682.

Zanos, T.P., Mineault, P.J., and Pack, C.C. (2011). Removal of spurious correlations between spikes and local field potentials. J. Neurophysiol. *105*, 474–486.

Zemankovics, R., Veres, J.M., Oren, I., and Hájos, N. (2013). Feedforward inhibition underlies the propagation of cholinergically induced gamma oscillations from hippocampal CA3 to CA1. J. Neurosci. *33*, 12337–12351.